Synergistic Cs/P Co-doping in Tubular g-C3N4 for Enhanced Photocatalytic Hydrogen Evolution

Juanfeng Gao , Xiao Lin * , Bowen Jiang , Haiyan Zhang , Youji Li

Posted Date: 3 June 2025

doi: 10.20944/preprints202506.0182.v1

Keywords: Cs/P Co-doping; Tubular g-C3N4; Synergistic Modification; Photocatalytic Hydrogen Evolution

 doi:10.20944/preprints202506.0182.v1

Article

Synergistic Cs/P Co-Doping in Tubular g-C_3N_4 for Enhanced Photocatalytic Hydrogen Evolution

Juanfeng Gao, Xiao Lin *, Bowen Jiang, Haiyan Zhang and Youji Li *

National Experimental Teaching Demonstration Center for Chemistry, College of Chemistry and Chemical Engineering, Jishou University, Jishou 416000, PR China

* Correspondence: linxiao2017@whu.edu.cn (X.L.); bcclyj@163.com (Y.L.)

Abstract: Developing high-performance photocatalysts for solar hydrogen production requires the synergistic modulation of chemical composition, nanostructure, and charge carrier transport pathways. Herein, we report a Cs and P co-doped tubular graphitic carbon nitride (Cs/PTCN-x) photocatalyst synthesized via a strategy that integrates elemental doping with morphological engineering. Structural characterizations reveal that phosphorus atoms substitute lattice carbon to form P-N bonds, while Cs^+ ions intercalate between g-C_3N_4 layers, collectively modulating surface electronic states and enhancing charge transport. Under visible-light irradiation ($\lambda \geq 420$ nm), the optimized Cs/PTCN-3 catalyst achieves an impressive hydrogen evolution rate of 8.085 $mmol \cdot g^{-1} \cdot h^{-1}$—over 33 times higher than that of pristine g-C_3N_4. This remarkable performance is attributed to the multidimensional synergy between band structure tailoring and hierarchical porous tubular architecture, which together enhance light absorption, charge separation, and surface reaction kinetics. This work offers a versatile approach for the rational design of g-C_3N_4-based photocatalysts toward efficient solar-to-hydrogen energy conversion.

Keywords: Cs/P Co-doping; tubular g-C_3N_4; synergistic modification; photocatalytic hydrogen evolution

1. Introduction

Hydrogen energy has emerged as a critical carbon-neutral energy vector, owing to its high energy density and zero-carbon emission characteristics. Nevertheless, conventional industrial hydrogen production methods (e.g., steam methane reforming) suffer from critical limitations including excessive energy requirements, economic impracticality, and unavoidable CO_2 byproducts, thereby compromising their environmental sustainability[1, 2]. In this context, visible-light-driven photocatalytic water splitting has gained prominence as a solar-to-fuel conversion strategy that simultaneously addresses energy security and environmental remediation. This technology employs semiconductor catalysts to directly harness solar energy for hydrogen evolution from water. While metal oxides (e.g., TiO_2, ZnO), sulfides (e.g., CdS), and oxyhalides have been widely investigated as photocatalysts[3, 4], their practical implementation remains constrained by inherent limitations such as narrow visible-light response ranges and photocorrosion susceptibility, both stemming from inappropriate bandgap configurations[5-7]. Graphitic carbon nitride (g-C_3N_4) has recently attracted significant attention in photocatalysis research due to its optimal bandgap (~2.7 eV), broad visible-light absorption spectrum, and earth-abundant precursor materials[8]. However, thermally polymerized g-C_3N_4 typically exhibits structural deficiencies, including low surface area, insufficient active sites, and rapid charge recombination, which collectively impair its photocatalytic hydrogen evolution performance.

To address these limitations, strategic modifications of g-C_3N_4 through morphology engineering and elemental doping have been actively pursued. Three-dimensional (3D) tubular architectures demonstrate particular promise, leveraging their high surface-to-volume ratios, abundant catalytic sites, and photon confinement effects to synergistically enhance light harvesting and charge carrier

 doi:10.20944/preprints202506.0182.v1

dynamics[9]. Wan et al.[10] developed hexagonal tubular g-C_3N_4 via supramolecular hydrogen-bonded self-assembly, achieving a 3.2-fold increase in visible-light absorption and 58% reduction in charge recombination compared to bulk counterparts. Similarly, Bi et al.[11] engineered hierarchically porous hollow tubes through hydrothermal synthesis, where the multiscale pore network simultaneously facilitated reactant diffusion and suppressed carrier migration pathways, ultimately reducing recombination efficiency by 73%. The unique optical waveguide behavior inherent to tubular geometries further extends photon-matter interaction lengths, enabling multi-reflective light harvesting that improves quantum efficiency by 41% at 450 nm, as quantitatively verified through finite-difference time-domain simulations.

Elemental doping has been established as a viable strategy to tailor the electronic properties of photocatalysts and enhance their catalytic performance. Specifically, the incorporation of alkali metal ions (e.g., Na^+, K^+) into graphitic carbon nitride (g-C_3N_4) effectively modulates its electronic structure through interlayer charge redistribution. Nevertheless, the optimization efficacy remains limited by ionic radius constraints inherent to alkali metals[12, 13]. Notably, Cs^+ doping demonstrates unique advantages due to its compatible ionic characteristics that enable effective doping while preserving the heptazine framework critical feature for maintaining structural integrity, as evidenced by recent studies[14]. In parallel, non-metallic element doping (e.g., phosphorus) modifies the band structure through P-N bond formation, thereby extending light absorption range. However, single-element doping systems face inherent limitations in achieving concurrent improvements in charge separation efficiency and surface reaction kinetics. This fundamental challenge has driven the emergence of multielement co-doping strategies, where synergistic optimization of bulk charge migration and interfacial catalytic processes presents a critical pathway toward high-performance photocatalysts.

Building on these insights, we developed a controllable strategy to incorporate Cs^+ ions into tubular g-C_3N_4 architectures via a soft-template-assisted in situ self-assembly approach. A three-dimensional supramolecular precursor was engineered by directing the oriented assembly of melamine-cyanurate units through phosphoric acid mediation. This methodology enables concurrent structural modulation and dopant integration during programmed thermal polycondensation. To unravel the synergistic effects of P-Cs co-doping on band structure engineering, charge carrier kinetics, and surface reaction pathways, we implemented a multimodal characterization framework combining optoelectronic correlation analysis with multiscale structural probes.

2. Experimental Section

2.1. Synthesis of P-Doped Tubular Carbon Nitride

Phosphorus-doped tubular carbon nitride was synthesized through a two-step process involving hydrothermal treatment followed by calcination, with melamine and phosphorus acid (H_3PO_4) as the starting materials. Briefly, a specific amount of melamine was dispersed in a 2 mol/L H_3PO_4 solution and stirred in a water bath at 60°C for 0.5 h. The resulting solution was then transferred into a Teflon-lined stainless steel autoclave and heated at 180°C for 10 h. After cooling to room temperature, the precipitate was collected, washed several times with deionized water, and dried at 60°C for 12 h, yielding the precursor material for tubular carbon nitride, denoted as Pre-PTCN. Finally, the Pre-PTCN was placed in a covered crucible and heated to 500°C at a rate of 2.5°C min^{-1} under an N_2 atmosphere, followed by maintaining the temperature for 4 h. The product was then naturally cooled to room temperature, yielding phosphorus-doped tubular g-C_3N_4, designated as P-TCN.

2.2. Synthesis of Cs-Doped Carbon Nitride

A mixture of 1.0 g melamine and cesium chloride (CsCl) was thoroughly ground in an agate mortar. The mixture was then transferred into a tube furnace and calcined at 500°C for 4 h under N_2 atmosphere with a heating rate of 2.5°C min^{-1}. After cooling to room temperature, the product was ultrasonically dispersed in deionized water, centrifuged and washed repeatedly to remove unreacted

 doi:10.20944/preprints202506.0182.v1

impurities, and dried at 60°C for 12 h in a vacuum oven to obtain Cs^+ modified bulk g-C_3N_4, denoted as CsCN. For comparative studies, pristine bulk g-C_3N_4 (labeled BCN) was synthesized under identical thermal conditions without CsCl addition.

2.3. Synthesis of P-Cs Co-Doped Tubular Carbon Nitride

For composite fabrication (Figure 1a), A homogeneous mixture containing 500 mg Pre-PTCN and 250 mg CsCl was prepared through thorough grinding. Subsequently, the mixture was transferred into an alumina crucible and calcined at 500°C for 4 h in a tube furnace under N_2 atmosphere, with a controlled heating rate of 2.5°C min^{-1}. After cooling to ambient temperature, the product underwent ultrasonic dispersion in deionized water, followed by three washing cycles with deionized water and vacuum drying at 60°C for 12 h, yielding Cs-P co-doped tubular g-C_3N_4 (denoted as Cs/PTCN-0.5). To systematically investigate composition-property relationships, a series of Cs/PTCN-x catalysts (x = 0.5, 1, 2, 3, 4) were synthesized by varying the mass ratios of CsCl to Pre-PTCN (0.5:1, 1:1, 2:1, 3:1, 4:1) while maintaining identical thermal treatment parameters.

Full details of the material characterizations, photoelectrochemical tests, and photocatalytic hydrogen experiments are provided in the Supplementary Material.

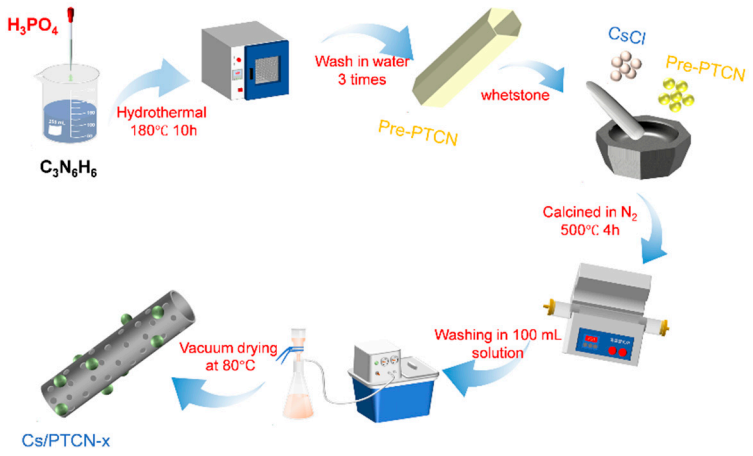

Figure 1. Synthesis diagram of Cs/PTCN-x composite materials.

3. Results and Discussion

3.1. Characterization of Material Structure

The phase composition and structural features of the materials were investigated through X-ray diffraction (XRD) analysis. As shown in Figure 2a, all samples (BCN, PTCN, CsCN, and Cs/PTCN-3) exhibit a characteristic (002) diffraction peak at 2θ = 27.5° (JCPDS 87-1526), corresponding to the graphitic-like interlayer stacking of g-C_3N_4. Both BCN and PTCN display an additional (100) diffraction peak at 2θ = 13.0°, originating from the in-plane periodic arrangement of heptazine units. Notably, the absence of discernible (100) peaks in CsCN and Cs/PTCN-3 indicates that Cs^+ incorporation significantly disrupts the ordered assembly during thermal polycondensation, consistent with the alkali metal-induced structural disordering mechanism reported in prior studies[15]. A distinct lattice expansion effect is observed in PTCN, manifested by a low-angle shift of the (002) peak (27.57° → 27.21°), which we attribute to partial substitution of lattice carbon by larger phosphorus atoms[16]. Conversely, CsCN and Cs/PTCN-3 demonstrate high-angle shifts of the (002) peak (27.57° → 27.63° and 28.20°, respectively), suggesting Cs^+ intercalation between g-C_3N_4 layers through K-N coordination bonds, thereby enhancing van der Waals interactions and reducing interlayer spacing[17]. The complete suppression of (100) diffraction in Cs-containing samples further confirms enhanced structural disorder induced by CsCl addition during thermal polymerization. No characteristic peaks corresponding to P or Cs-containing phases are detected, implying that dopants

 doi:10.20944/preprints202506.0182.v1

either exist in non-crystalline forms (<5 wt% by EDS) or are intercalated within the g-C_3N_4 matrix without forming discrete compounds[15].

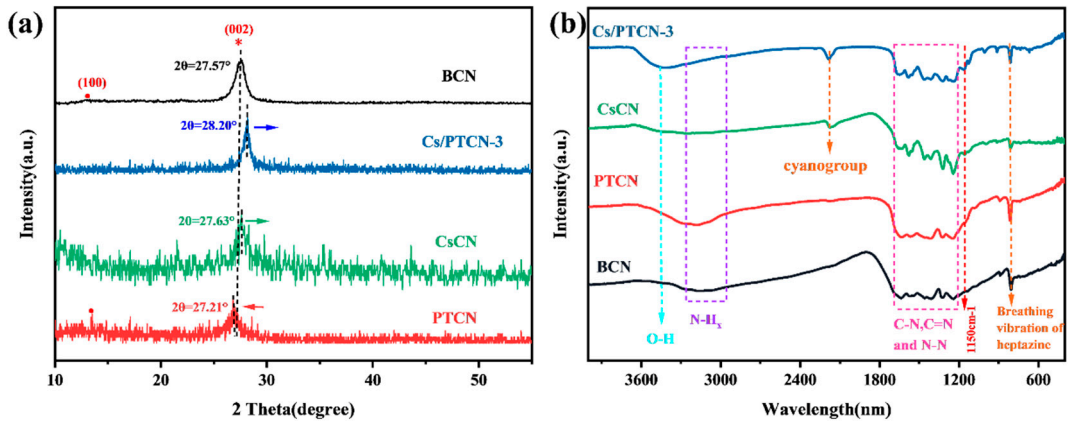

Figure 2. XRD patterns (a) and FT-IR spectra (b) of BCN, CsCN, PTCN, and Cs/PTCN-3 catalysts.

The chemical bond structures of BCN, PTCN, CsCN, and Cs/PTCN-3 catalysts were analyzed using Fourier-transform infrared (FT-IR) spectroscopy, as shown in Figure 2b. All samples exhibit characteristic g-C_3N_4 absorption signatures, confirming that the introduction of P and Cs preserves the fundamental structural motifs of g-C_3N_4, consistent with XRD structural analyses. Among the observed peaks, a peak at 810 cm^{-1} corresponding to out-of-plane bending vibrations of heptazine rings, verifying the structural integrity of the heptazine framework. Multiple absorption bands in the 1200-1600 cm^{-1} range attributed to C-N, C=N, and N-N stretching vibrations, characteristic of the conjugated aromatic system in g-C_3N_4. Broad features at 3000-3400 cm^{-1} (N-H stretching) and 3500 cm^{-1} (O-H vibration from adsorbed water)[18, 19]. Notably, CsCN and Cs/PTCN-3 display an emergent absorption band at 2175 cm^{-1}, assigned to C≡N stretching vibrations (-C≡N groups). Comparative analysis reveals enhanced intensity of the C-O asymmetric vibration at 1150 cm^{-1} relative to BCN, suggesting electronic modulation induced by P-Cs co-doping. The combined XRD and FT-IR evidence demonstrates that P-Cs dual modification synergistically tunes surface functionalities and electronic configurations while maintaining g-C_3N_4 structural framework. This precise structural engineering establishes critical foundational features for enhanced photocatalytic performance[20].

The surface and microstructures of the catalyst materials were characterized using scanning electron microscopy (SEM) and transmission electron microscopy (TEM), as shown in Figure 3(a-h). As revealed by morphological analysis (Figure 3a), pristine BCN exhibits a dense lamellar architecture with characteristic bulk stacking between adjacent layers. In contrast, PTCN demonstrates well-defined hollow tubular structures (2-3 μm diameter) featuring smooth surfaces, formed through controlled thermal decomposition of H_3PO_4-mediated melamine-cyanurate supramolecular precursors. During calcination, the oriented π-π stacked precursors undergo progressive shrinkage accompanied by NH_3/CO_2 gas evolution, ultimately yielding intact tubular morphology[10]. Remarkably, Cs/PTCN-3 maintains this structural framework while developing surface roughening and mesoporous features (Figure 3d). This synergistic morphological evolution enhances both specific surface area (BET analysis in Figure S2) and accessible active sites, thereby significantly boosting photocatalytic activity through improved reactant adsorption and charge carrier utilization efficiency.

 doi:10.20944/preprints202506.0182.v1

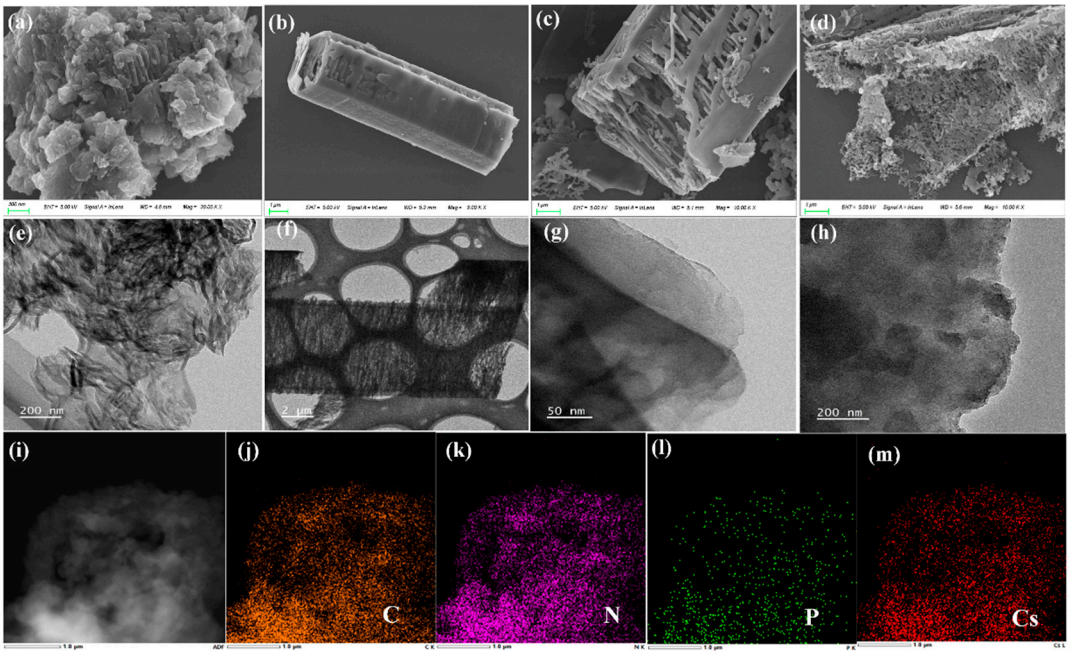

Figure 3. SEM images of (a) BCN, (b-c) PTCN, and (d) Cs/PTCN-3; TEM images of (e) BCN, (f-g) PTCN, and (h) Cs/PTCN-3, (i-m) Corresponding elemental mapping images of C, N, P, and Cs elements.

Additionally, the energy-dispersive X-ray (EDX) elemental mapping of Cs/PTCN-3 (Figure 3i-m) demonstrates the uniform distribution of C, N, P, and Cs elements within the selected region, confirming the successful doping of P and Cs in Cs/PTCN-3. Quantitative EDS analysis (Table S1) reveals atomic percentages of 64.18% C, 33.91% N, 0.03% P, and 1.88% Cs, verifying precise control over composite stoichiometry during synthesis. These engineered morphological and structural modifications synergistically enhance photocatalytic performance through dual mechanisms: (1) surface roughening and pore structure significantly increase the exposure density of active sites; (2) the light wave effect of the tubular morphology extends the propagation path of the incident light inside the material, which leads to the enhancement of the visible light absorption efficiency. These properties provide a fundamental structural basis for the excellent activity of Cs/PTCN-3 in the photocatalytic hydrogen precipitation reaction.

The electronic structures and chemical states of the elements in BCN, PTCN, and Cs/PTCN-3 catalysts were further analyzed using X-ray photoelectron spectroscopy (XPS). The XPS survey spectra (Figure 4a) reveal that all catalysts predominantly consist of C, N, and O elements. Distinct Cs characteristic peaks are observed in Cs/PTCN-3, confirming successful Cs incorporation. However, P signals remain weak in the full spectrum due to its low concentration. High-resolution XPS spectra (Figure 4b-d) demonstrate similar profiles for BCN, PTCN, and Cs/PTCN-3. For Cs/PTCN-3, the C 1s spectrum deconvolutes into three peaks at 284.8 eV (adventitious carbon), 286.62 eV (edge-terminated C-NH_x in tri-s-triazine structures), and 288.43 eV (sp^2-hybridized carbon in N-C=N aromatic rings)[21]. The N 1s spectrum exhibits three binding energies: 398.88 eV (C-N=C), 400.63 eV (N-$(C)_3$), and 401.42 eV (C-NH_2)[22]. Both C 1s and N 1s peaks exhibit slight shifts toward lower binding energies compared to BCN, likely due to partial substitution of sp^2-carbon by phosphorus atoms, which increases electron density within heptazine units.

 doi:10.20944/preprints202506.0182.v1

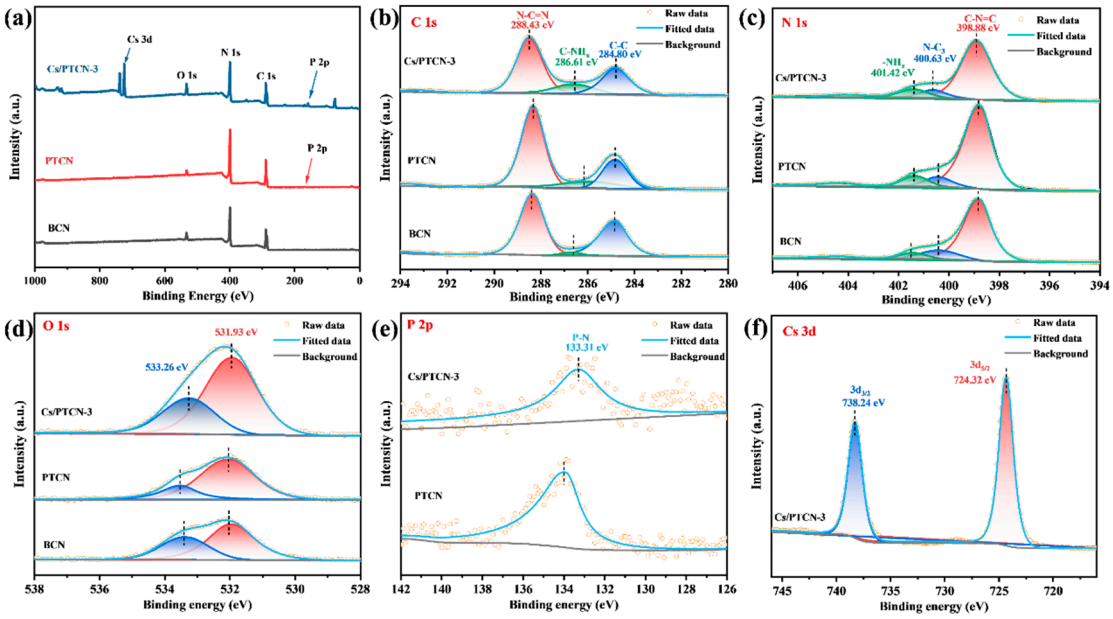

Figure 4. (a) XPS survey spectra and high-resolution spectra of (b) C 1s, (c) N 1s, (d) O 1s, (e)P 2p, and (f) Cs 3d for BCN, PTCN, and Cs/PTCN-3 catalysts.

The O 1s spectrum deconvolutes into two peaks at 531.93 eV (C=O) and 533.26 eV (C-O), originating from adsorbed CO_2 or surface-oxygenated functional groups[23]. Although no distinct P 2p signal appears in the full spectrum, the characteristic P-N peak at 133.32 eV confirms successful P doping through covalent bond formation between phosphorus and neighboring nitrogen atoms via P substitution for C atoms in the carbon nitride matrix[24, 25]. Furthermore, the Cs 3d doublet at 738.24 eV ($3d_{3/2}$) and 724.32 eV ($3d_{5/2}$) in Cs/PTCN-3 unambiguously confirms Cs^+ oxidation state[26]. Given the +1 valence and substantially larger ionic radius of Cs^+ compared to C/N atoms in carbon nitride (precluding direct lattice substitution), Cs^+ likely resides either through electrostatic adsorption on heptazine rings or interlayer intercalation. These results demonstrate that Cs/PTCN-3 maintains the intrinsic carbon nitride framework while optimizing surface chemical states and introducing active sites via Cs-P co-doping synergism, thereby establishing critical foundations for enhanced photocatalytic performance.

3.2. Optical Properties and Charge Carrier Behavior

The optical properties of the catalysts were evaluated using UV-Vis diffuse reflectance spectroscopy (UV-Vis DRS), and the results are presented in Figure 5a. All modified photocatalysts exhibit distinct red shifts in their intrinsic absorption edges compared to BCN[27]. The intrinsic absorption edge of BCN lies near 450 nm, while that of P-doped PTCN shows a slight red shift, indicating that P incorporation extends the visible-light absorption range of carbon nitride. Upon Cs intercalation, CsCN demonstrates a further red-shifted absorption edge to 470 nm, thereby achieving enhanced light-harvesting capability. Notably, Cs/PTCN-3 exhibits a blue shift relative to CsCN, which arises from the synergistic effects of Cs-P dual doping and its unique interfacial architecture, collectively improving photon capture efficiency. The bandgap values of all photocatalysts, derived via the Kubelk-Munk equation ($\alpha h\nu = A(h\nu - Eg)^{1/2}$), are determined as 2.70, 2.64, 2.52, and 2.60 eV for BCN, PTCN, CsCN, and Cs/PTCN-3, respectively (Figure 5b). These results demonstrate that P-Cs co-doping enables precise modulation of carbon nitride's band structure, effectively broadening the photoresponse range and enhancing light utilization efficiency, which collectively contribute to improved photocatalytic performance.

 doi:10.20944/preprints202506.0182.v1

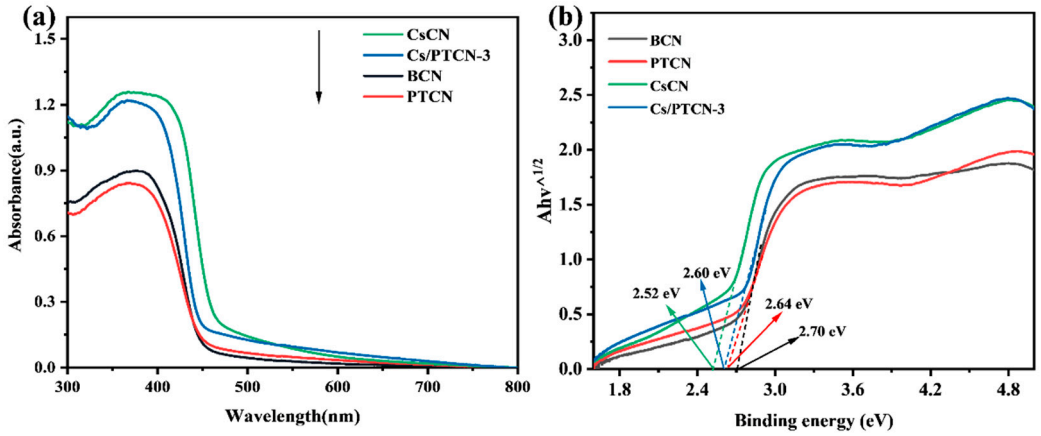

Figure 5. (a) UV-Vis DRS spectra and (b) E_g value.

The photogenerated carrier behavior of the catalysts under illumination was investigated through steady-state photoluminescence (PL) spectroscopy, as shown in Figure 6a. All materials exhibit distinct fluorescence emission peaks at 420-550 nm, attributed to electron-hole (e^-/h^+) pair recombination in the photocatalysts. Compared to BCN, PTCN demonstrates reduced PL intensity due to quantum confinement effects induced by the porous tubular structure, which facilitates charge transfer and suppresses carrier recombination. Notably, Cs/PTCN-3 exhibits the lowest PL peak intensity near 460 nm compared to BCN, PTCN, and CsCN. This indicates that the introduction of P and Cs not only enhances charge diffusion rates within the π-conjugated system but also promotes interlayer charge transport via Cs^+ intercalation, significantly improving photogenerated carrier separation efficiency[28]. These results demonstrate that the dual optimization strategy combining morphological engineering with P-Cs co-modification achieves superior charge separation and utilization through simultaneous construction of charge transfer channels and electronic structure modulation, ultimately enhancing photocatalytic hydrogen evolution performance.

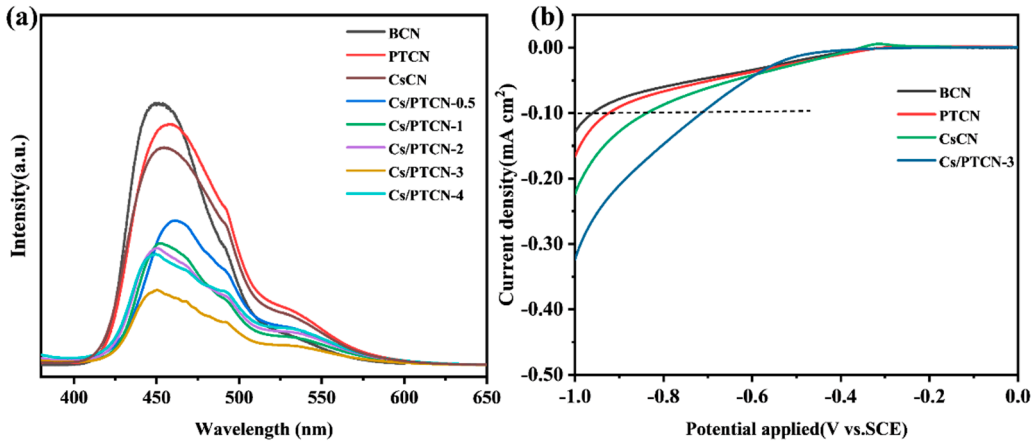

Figure 6. (a) PL spectra and (b) LSV spectra for BCN, PTCN, CsCN, and Cs/PTCN-x catalysts.

As shown in the LSV polarization curves (Figure 6b), BCN exhibits a large overpotential, confirming its low hydrogen evolution activity. P doping in PTCN markedly reduces this overpotential. The synergistic P-Cs co-modification in Cs/PTCN-3 yields the lowest overpotential, demonstrating that elemental doping and morphological engineering collaboratively enhance electron transfer kinetics and proton reduction efficiency during the hydrogen evolution reaction.

The transport and transfer behavior of photogenerated carriers in the photocatalysts was further investigated through electrochemical analysis. As shown in Figure 7a, all modified carbon nitride

 doi:10.20944/preprints202506.0182.v1

samples exhibit enhanced photocurrent intensities, with Cs/PTCN-3 demonstrating the highest response. This improvement can be attributed to the synergistic modifications, which reduce charge diffusion distances, enhance charge separation/transfer efficiency, accelerate bulk-to-surface carrier migration, and suppress electron-hole (e^-/h^+) pair recombination, thereby boosting hydrogen evolution performance. Electrochemical impedance spectroscopy (EIS) was employed to evaluate charge transfer resistance, where a smaller Nyquist arc radius corresponds to lower interfacial resistance and higher e^-/h^+ separation efficiency. As evidenced in Figure 7b, Cs/PTCN-3 exhibits the smallest arc radius among all samples, indicating minimal charge transfer resistance. Comparative analysis reveals that P doping and Cs^+ intercalation significantly reduce surface charge transfer resistance relative to pristine BCN, while improving carrier separation and migration efficiency. These electrochemical enhancements directly correlate with the superior photocatalytic hydrogen evolution activity observed in Cs/PTCN-3.

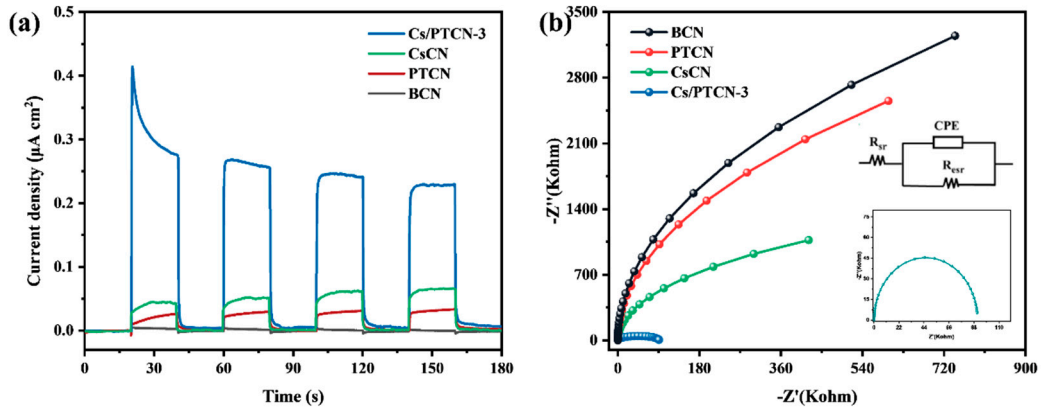

Figure 7. (a) Transient I-t curves and (b) EIS Nyquist plots for BCN, PTCN, CsCN, and Cs/PTCN-3 catalysts.

3.3. Evaluation of Photocatalytic Hydrogen Evolution Performance

To evaluate the photocatalytic performance, hydrogen evolution reaction (HER) experiments were conducted under visible light irradiation ($\lambda \geq 400$ nm) using methanol (CH_3OH) as a sacrificial agent. Figure 8a displays the time-dependent H_2 production profiles of BCN, PTCN, CsCN, and Cs/PTCN-3 composite catalysts under visible light illumination. As shown in Figure 8b, BCN exhibits the lowest photocatalytic HER activity, with an average hydrogen evolution rate of merely 0.138 $mmol \cdot g^{-1} \cdot h^{-1}$ over 4 hours. In contrast, PTCN and CsCN demonstrate improved photocatalytic performance, achieving rates of 0.336 and 0.705 $mmol \cdot g^{-1} \cdot h^{-1}$, respectively. Remarkably, Cs/PTCN-3 shows significantly enhanced activity, reaching a HER rate of 8.085 $mmol \cdot g^{-1} \cdot h^{-1}$, which is 33-, 22-, and 11.5-fold higher than those of BCN, PTCN, and CsCN, respectively. This enhancement originates from multiscale synergistic mechanisms: (1) The hollow tubular structure mitigates interlayer agglomeration in g-C_3N_4, substantially increasing the specific surface area and exposing more active HER sites; (2) Cs^+ intercalation creates interlayer charge transport pathways, enhancing photogenerated carrier mobility and separation efficiency.

Furthermore, the light-to-energy conversion efficiency was quantitatively evaluated through apparent quantum efficiency (AQE) measurements (Figure 8c). The AQE trend exhibits a positive correlation with the photocatalytic hydrogen evolution rate. Cs/PTCN-3 was found to achieve an AQE of 18.38%, representing 58-fold and 12.8-fold enhancements compared to BCN (0.314%) and PTCN (1.435%), respectively. These results demonstrate that the synergistic strategy combining P-doping and Cs^+ modification significantly enhances photocatalytic hydrogen evolution performance by precisely regulating the electronic structure, morphology, and interfacial charge behavior of carbon nitride. Beyond photocatalytic activity, catalyst stability during prolonged operation is critical for assessing practical applicability. The durability of Cs/PTCN-3 was investigated through continuous photocatalytic water splitting experiments over 10 hours. As shown in Figure 8d, the

 doi:10.20944/preprints202506.0182.v1

catalyst maintains stable hydrogen evolution rates throughout the extended reaction period, confirming its robust operational stability.

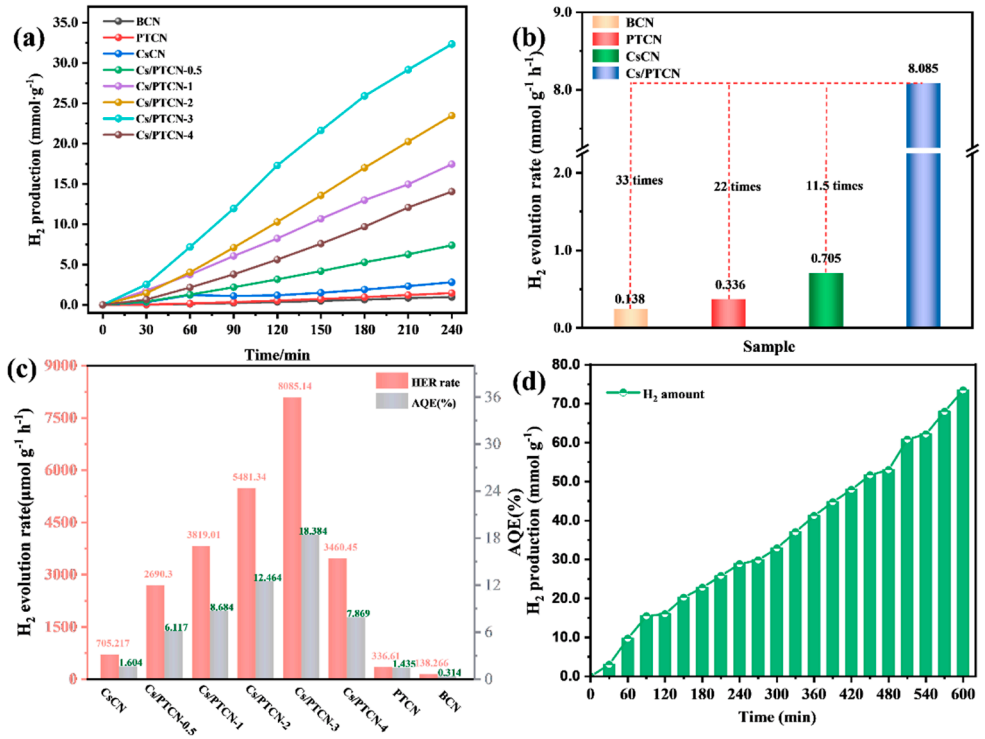

Figure 8. (a) Photolytic water hydrogen precipitation performance of different catalysts, (b) Comparison of average hydrogen precipitation rates, (c) Hydrogen production rates and apparent quantum efficiencies of the catalysts, and (d) Stability test of Cs/PTCN-3.

After repeated centrifugation and washing of the post-reaction material until the supernatant reached neutral pH, the catalyst was redispersed in 50 mL of 20 vol% methanol aqueous solution for hydrogen evolution testing (Figure 9a, run 2). The Cs/PTCN-3 catalyst exhibited a hydrogen yield of 31.82 mmol·g^{-1} corresponding to 96.8% of its initial activity (32.34 mmol·g^{-1}), demonstrating retained hydrogen evolution efficacy. FT-IR spectra of Cs/PTCN-3 before and after illumination (Figure 9b) reveal no significant alterations in characteristic absorption peaks, confirming negligible chemical restructuring during photocatalytic cycling and exceptional structural stability. Furthermore, comparative analysis with literature-reported photocatalysts (Figure S3) highlights the competitive advantage of Cs/PTCN-3 in hydrogen evolution performance.

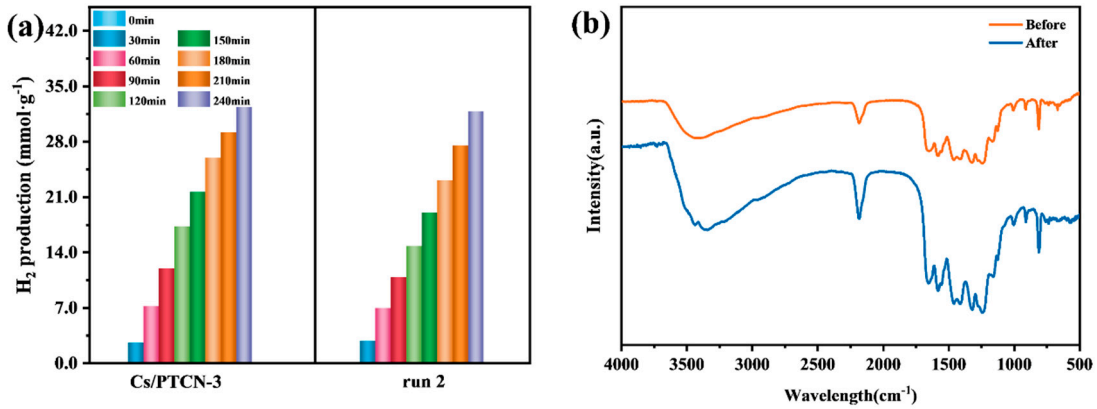

Figure 9. (a) Stability test of Cs/PTCN-3, (b) FT-IR spectra of Cs/PTCN-3 before and after cycles of experiments.

 doi:10.20944/preprints202506.0182.v1

3.4. Proposed Photocatalytic Mechanism

The appropriate conduction band (CB), valence band (VB), and band structure of the catalysts are critical factors governing photocatalytic reactions, which can be derived from Mott-Schottky measurements. As shown in Figure 10(a-d), all four materials exhibit positive slopes in their Mott-Schottky plots, confirming their n-type semiconductor characteristics and indicating that doping preserves the semiconducting nature of carbon nitride[29]. The flat-band potentials ($E_{Ag/AgCl}$) of BCN, PTCN, CsCN, and Cs/PTCN-3 versus Ag/AgCl were determined as -1.2, -1.16, -0.85, and -1.01 V, respectively. These values correspond to standard hydrogen electrode (NHE) potentials of -1.003, -0.963, -0.653, and -0.813 V vs NHE ($E_{NHE} = E_{Ag/AgCl} + 0.197$)[30, 31]. Given that the CB positions approximately equal the flat-band potentials, the calculated CB values for BCN, PTCN, CsCN, and Cs/PTCN-3 are -1.003, -0.963, -0.653, and -0.813 eV, respectively. Using the relationship between VB, CB, and bandgap ($E_{VB}=E_g-E_{CB}$), the VB positions are derived as 1.697, 1.677, 1.867, and 1.787 eV for BCN, PTCN, CsCN, and Cs/PTCN-3, respectively.

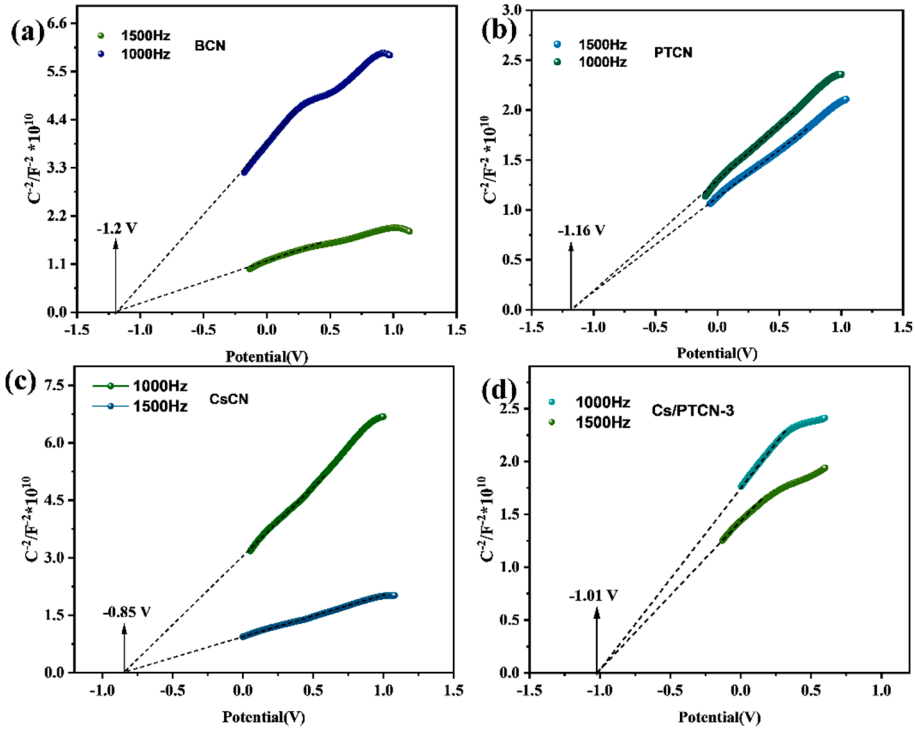

Figure 10. Mott-Schottky plots of (a) BCN, (b) PTCN, (c) CsCN, (d) Cs/PTCN-3.

Based on the photocatalytic performance evaluations and material characterization results, a plausible mechanism for visible-light-driven water splitting and hydrogen evolution on Cs/PTCN-3 is proposed, as illustrated in Figure 11b. Under visible-light irradiation, electrons in the valence band (VB) of Cs/PTCN-3 are photoexcited to the conduction band (CB), generating electron-hole pairs. While a majority of these charge carriers recombine radiatively through photon emission, a fraction undergoes multi-pathway migration to the catalyst surface for redox reactions: (1) P doping disrupts the planar periodicity of g-C_3N_4, inducing lattice distortion that effectively reduces charge migration barriers and accelerates charge separation; (2) Cs^+ intercalation simultaneously modulates the electronic structure and establishes interlayer charge transport channels, enhancing interlayer carrier separation/transfer efficiency while suppressing recombination. Concurrently, the material's unique architecture amplifies reaction interfaces and active site density, thereby accelerating proton/electron transfer kinetics. The synergistic interplay between electronic structure engineering and morphological optimization significantly enhances charge separation efficiency, ultimately enabling efficient and stable hydrogen evolution under visible light.

 doi:10.20944/preprints202506.0182.v1

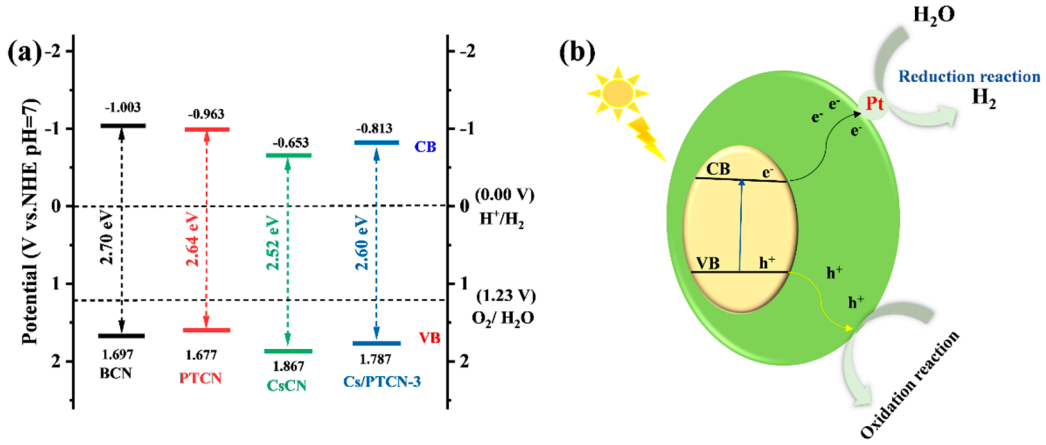

Figure 11. BCN, PTCN, CsCN, Cs/PTCN-3 of (a) energy band structure, and (b) photocatalytic mechanism of Cs/PTCN-3.

4. Conclusions

In this study, a Cs/PTCN composite catalyst with efficient visible-light-driven photocatalytic hydrogen production performance was successfully fabricated through a synergistic modification strategy involving morphological regulation, non-metallic phosphorus doping, and cesium ion (Cs^+) intercalation. The results demonstrate that phosphorus atoms form P-N bonds by substituting lattice carbon, disrupting the planar periodic structure of g-C_3N_4, significantly reducing charge carrier migration barriers, and promoting charge separation. Simultaneously, Cs^+ intercalation not only modulates the electronic structure of the material but also provides efficient channels for interlayer charge transport, enhancing the separation and transfer efficiency of photogenerated carriers. Furthermore, the unique tubular porous morphology accelerates charge transfer kinetics by expanding the reaction interface and active site density. Under visible light irradiation ($\lambda \geq 420$ nm), Cs/PTCN-3 exhibits an exceptional hydrogen evolution rate of 8.085 mmol·g^{-1}·h^{-1} (AQE = 18.38%), which is 33-fold and 22-fold higher than BCN and PTCN, respectively, while maintaining stable performance over a 10-hour cyclic test. This work provides an innovative strategy for the multidimensional synergistic regulation of the structure and properties of g-C_3N_4-based photocatalysts, offering significant insights for developing high-efficiency photocatalytic hydrogen production systems.

Supplementary Materials: The following supporting information can be downloaded at the website of this paper posted on Preprints.org.

Acknowledgments: We acknowledge the financial support for this work by the Natural Science Foundation of Hunan Province (2024JJ7401), Natural Science Research Project of Jishou University (No. Jd21010), Doctoral Research Startup Fund of Jishou University, and the Postgraduate Research Innovation Project of Jishou University (Jdy23010).

References

1. Gunawan, D.; Zhang, J. J.; Li, Q. Y.; et al. Materials Advances in Photocatalytic Solar Hydrogen Production: Integrating Systems and Economics for a Sustainable Future. *Advanced Materials* **2024**, *36*, 2404618. DOI: 10.1002/adma.202404618.
2. Zhou, P.; Ahmed Navid, I.; Ma, Y. J.; et al. Solar-to-hydrogen Wfficiency of More Than 9% in Photocatalytic Water Splitting. *Nature* **2023**, *613*, 66-70. DOI: 10.1038/s41586-022-05399-1.
3. Verma, G.; Islam, M.; Gupta, A. ZnO nanowire-decorated 3D printed pyrolytic carbon for solar light-driven photocatalytic degradation of wastewater contaminants. *Advanced Composites and Hybrid Materials* **2025**, *8* (1), 109. DOI: 10.1007/s42114-024-01125-9.

 doi:10.20944/preprints202506.0182.v1

4. Lan, R. M.; Hu, Z. F.; Liu, H. R.; et al. Passivating Lattice Oxygen in ZnO Nanocrystals to Reduce its Interactions with the Key Intermediates for a Selective Photocatalytic Methane Oxidation to Methanol. *Angewandte Chemie International Edition* **2025**, *64* (14), e202425186. DOI: 10.1002/anie.202425186.
5. Wu, Y. H.; Yan, Y. Q.; Deng, Y. X.; et al. Rational construction of S-scheme CdS quantum dots/In_2O_3 hollow nanotubes heterojunction for enhanced photocatalytic H_2 evolution. *Chinese Journal of Catalysis* **2025**, *70*, 333-340. DOI: 10.1016/s1872-2067(24)60213-5.
6. Sun, R. J.; Zhu, Z. J.; Tian, N.; et al. Hydrogen Bonds and In situ Photoinduced Metallic Bi^0/Ni^0 Accelerating Z-Scheme Charge Transfer of BiOBr@NiFe - LDH for Highly Efficient Photocatalysis. *Angewandte Chemie International Edition* **2024**, *63* (41), e202408862. DOI: 10.1002/anie.202408862.
7. Chen, Y. H.; Zhang, L.; Chen, S.; et al. Synthesis of Heteromorphic Bi_2WO_6 Films With an Interpenetrate 1D/2D Network Structure for Efficient and Stable Photocatalytic Degradation of VOCs. *Advanced Materials* **2024**, *36* (40), 2407400. DOI: 10.1002/adma.202407400.
8. Li, L.; Zhou, Z. P.; Shi, Y.; et al. Donor–Acceptor Type Carbon Nitride Photocatalysts in Photocatalysis: Current Understanding, Applications and Challenges. *Small* **2025**, *21* (8), 2409903. DOI: 10.1002/smll.202409903.
9. Pan, Y. L.; Zhang, Q.; Huang, G. Z.; et al. Efficient photocatalytic H_2 evolution over tubular mesoporous carbon nitride with N-vacancy by microwave-assisted synthesis. *Science China Chemistry* **2025**, *68*, 866–873. DOI: 10.1007/s11426-024-2237-1.
10. Wan, S. P.; Ou, M.; Wang, Y. N.; et al. Protonic acid-assisted universal synthesis of defect abundant multifunction carbon nitride semiconductor for highly-efficient visible light photocatalytic applications. *Applied Catalysis B: Environmental* **2019**, *258*, 118011. DOI: 10.1016/j.apcatb.2019.118011.
11. Bi, L. B.; Shen, J. M.; Yan, P. W.; et al. Efficient photodegradation of micropollutants by tubular carbon nitride: The role of nitrogen defects. *Journal of Cleaner Production* **2023**, *419* (138328). DOI: 10.1016/j.jclepro.2023.138328.
12. Yue, J. P.; Yang, H. P.; Zhou, L.; et al. H_2O_2 photosynthesis on doubly heteroatom (K and Na) intercalated carbon nitride: Collaboration and division of boosting in-layer and inter-layer carrier transfer. *Chemical Engineering Journal* **2025**, *505*, 159434. DOI: 10.1016/j.cej.2025.159434.
13. Palani, G.; Apsari, R.; Hanafiah, M. M.; et al. Metal-Doped Graphitic Carbon Nitride Nanomaterials for Photocatalytic Environmental Applications—A Review. *Nanomaterials* **2022**, *12* (10), 1754. DOI: 10.3390/nano12101754.
14. Zhang, Q. Y.; Chen, C. C.; Liu, F. T.; et al. Elucidating the tandem synergistic roles of Cs-O dual sites confined in carbon nitride toward selective photoreduction H_2O_2 production coupled with xylose oxidation. *Chemical Engineering Journal* **2025**, *509*, 161204. DOI: 10.1016/j.cej.2025.161204.
15. Tahereh, M. S.; Hossein, F.; Byeong Kyu, L.; et al. Caesium sites coordinated in Boron-doped porous and wrinkled graphitic carbon nitride nanosheets for efficient charge carrier separation and Transfer: Photocatalytic H_2 and H_2O_2 production. *Chemical Engineering Journal* **2021**, *423*, 130067. DOI: 10.1016/j.cej.2021.130067.
16. Ran, J. R.; Ma, T. Y.; Gao, G. P.; et al. Porous P-doped graphitic carbon nitride nanosheets for synergistically enhanced visible-light photocatalytic H_2 production. *Energy & Environmental Science* **2015**, *8* (12), 3708-3717. DOI: 10.1039/c5ee02650d.
17. Liu, Q.; Li, H.; Zhang, H.; et al. The role of Cs dopants for improved activation of molecular oxygen and degradation of tetracycline over carbon nitride. *Chinese Chemical Letters* **2022**, *33* (11), 4756-4760. DOI: 10.1016/j.cclet.2021.12.089.
18. Tong, H. J.; Odutola, J.; Song, J. S.; et al. Boosting the Quantum Efficiency of Ionic Carbon Nitrides in Photocatalytic H_2O_2 Evolution via Controllable $n \rightarrow \pi^*$ Electronic Transition Activation. *Advanced Materials* **2024**, *36* (49), 2412753. DOI: 10.1002/adma.202412753.
19. Qin, J. N.; Barrio, J.; Peng, G. M.; et al. Direct growth of uniform carbon nitride layers with extended optical absorption towards efficient water-splitting photoanodes. *Nature Communications* **2020**, *11* (1), 4701. DOI: 10.1038/s41467-020-18535-0.

 doi:10.20944/preprints202506.0182.v1

20. You, Z. Y.; Li, G.; Wang, C. H.; et al. The synergistic effect of potassium ions and nitrogen defects on carbon nitride for enhanced photocatalytic hydrogen evolution. *International Journal of Hydrogen Energy* **2023**, *48* (42), 15934-15943. DOI: 10.1016/j.ijhydene.2023.01.089.
21. Dong, J. T.; Zhao, J. Z.; Yan, X. W.; et al. Construction of carbonized polymer dots/potassium doped carbon nitride nanosheets Van der Waals heterojunction by ball milling method for facilitating photocatalytic CO_2 reduction performance in pure water. *Applied Catalysis B: Environment and Energy* **2024**, *351*, 123993. DOI: 10.1016/j.apcatb.2024.123993.
22. Zhang, Y.; Zhai, M. m.; Liu, J.; et al. Anchoring Ag Atom on Carbon Vacancy Enriched Carbon Nitride to Synergistically Promote CO_2 Photoredution with Water. *Advanced Functional Materials* **2024**, *35* (3), 2413232. DOI: 10.1002/adfm.202413232.
23. Jiang, M.; Zhu, Y. x.; Jia, Z. t.; et al. Boron and Oxygen Dual‐Doped Carbon Nitride Nanotubes with Frustrated Lewis Pairs for Efficient Electrocatalytic Ammonia Synthesis. *Small Methods* **2024**, 2401672. DOI: 10.1002/smtd.202401672.
24. Liu, Z. G.; Zhang, X.; Jiang, Z. X.; et al. Phosphorus and sulphur co-doping of g-C_3N_4 nanotubes with tunable architectures for superior photocatalytic H_2 evolution. *International Journal of Hydrogen Energy* **2019**, *44* (36), 20042-20055. DOI: 10.1016/j.ijhydene.2019.06.037.
25. Jang, D.; Lee, S.; Kwon, N. H.; et al. Preparation of carbon nitride nanotubes with P-doping and their photocatalytic properties for hydrogen evolution. *Carbon* **2023**, *208*, 290-302. DOI: 10.1016/j.carbon.2023.03.038.
26. Adnan, M.; Lee, W.; Irshad, Z.; et al. Managing Interfacial Defects and Charge‐Carriers Dynamics by a Cesium‐Doped SnO_2 for Air Stable Perovskite Solar Cells. *Small* **2024**, *20* (37), 2402268. DOI: 10.1002/smll.202402268.
27. Wu, B. G.; Jiang, B. J.; Guo, C. L.; et al. Mild-Condition Photocatalytic Reforming of Methanol-Water by a Hierarchical, Asymmetry Carbon Nitride. *Angewandte Chemie International Edition* **2024**, *64* (6), 6525-6534. DOI: 10.1002/anie.202418677.
28. Ma, M. M.; Li, J. Z.; Zhu, X. G.; et al. Enhancing multifunctional photocatalysis with acetate-assisted cesium doping and unlocking the potential of Z-scheme solar water splitting. *Carbon Energy* **2023**, *6* (3), e447. DOI: 10.1002/cey2.447.
29. Fang, H. X.; Guo, H.; Niu, C. G.; et al. Hollow tubular graphitic carbon nitride catalyst with adjustable nitrogen vacancy: Enhanced optical absorption and carrier separation for improving photocatalytic activity. *Chemical Engineering Journal* **2020**, *402*, 126185. DOI: 10.1016/j.cej.2020.126185.
30. Du, J.; Li, S. M.; Du, Z. G.; et al. Boron/oxygen-codoped graphitic carbon nitride nanomesh for efficient photocatalytic hydrogen evolution. *Chemical Engineering Journal* **2021**, *407*, 127114. DOI: 10.1016/j.cej.2020.127114.
31. Ali, A.; Tsuyoshi, M.; Sagiri, W.; et al. Determination of enantiomeric excess of carboxylates by fluorescent macrocyclic sensors. *Chemical Science* **2016**, *7* (3), 2016-2022. DOI: 10.1039/c5sc04235f.